

Magnifying Networks for Images with Billions of Pixels

Neofytos Dimitriou Ognjen Arandjelović
University of St Andrews
KY16 9SX, United Kingdom

neofyotosd, ognjen.arandjelovic@gmail.com

Abstract

The shift towards end-to-end deep learning has brought unprecedented advances in many areas of computer vision. However, there are cases where the input images are excessively large, deeming end-to-end approaches impossible. In this paper, we introduce a new network, the Magnifying Network (MagNet), which can be trained end-to-end independently of the input image size. MagNets combine convolutional neural networks with differentiable spatial transformers, in a new way, to navigate and successfully learn from images with billions of pixels. Drawing inspiration from the magnifying nature of an ordinary brightfield microscope, a MagNet processes a downsampled version of an image, and without supervision learns how to identify areas that may carry value to the task at hand, upsamples them, and recursively repeats this process on each of the extracted patches. Our results on the publicly available Camelyon16 and Camelyon17 datasets first corroborate to the effectiveness of MagNets and the proposed optimization framework and second, demonstrate the advantage of Magnets' built-in transparency, an attribute of utmost importance for critical processes such as medical diagnosis.

1. Introduction

Convolutional neural networks (CNNs) have been the major drive behind the paradigm shift of computer vision towards deep learning. Over the years, the research community has come up with a cornucopia of convolution-based network topologies with differences in their connectivity patterns, training procedures, and building blocks [32, 15, 34, 39, 17, 6, 24, 18, 30]. As a consequence of the continuous improvements and the widespread availability of annotated data [9, 21, 23, 12, 26, 1, 8], end-to-end trained CNNs have dominated the area of visual object recognition.

In parallel with the increase in data availability, hardware advancements have created the possibility of both the capturing and storing of much larger images. One of the most extreme yet practically important examples can be

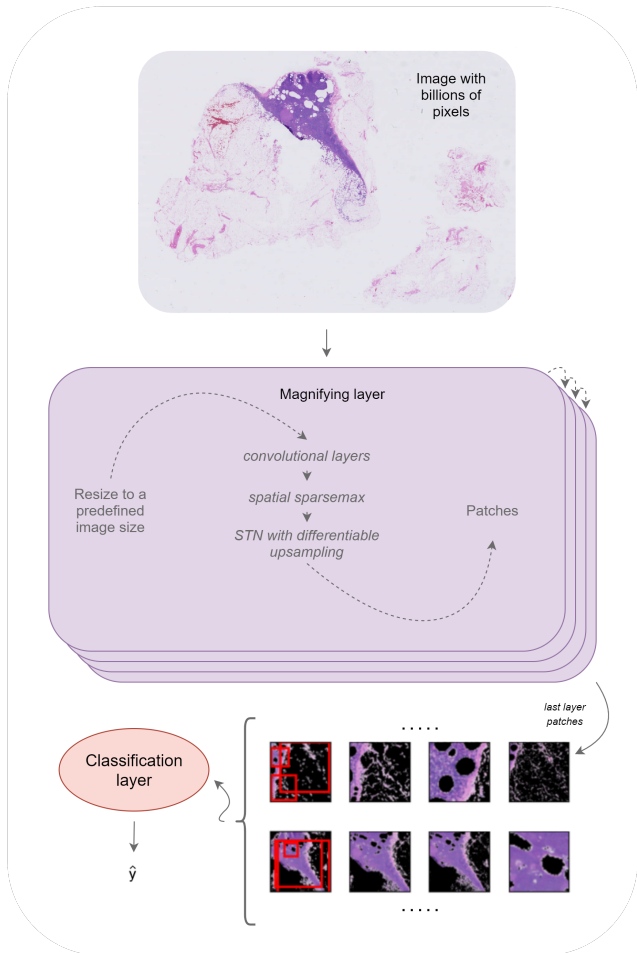


Figure 1. An Illustration of the architecture of MagNet. The shown model consists of 3 magnifying layers and a classification layer.

found in Digital Pathology and in particular, in the task of analysing so-called whole slide images (WSIs) [10, 4] – digitized microscope slides which are often several gigabyte in size with a typical resolution of 100000×100000 pixels [38, 10]. Conventional neural network optimization using such images is practically infeasible considering the

associated memory and compute requirements.

In this paper, we introduce a new family of neural networks, henceforth referred to as Magnifying Networks (MagNets), that can be optimized end-to-end even when the input images have billions of pixels. MagNets use an attention based mechanism to decide on a course to fine basis when to analyse increasingly finer-grain detail as a way of processing extremely large images (n.b. incidentally, this is conceptually similar to a pathologist’s knowledge and attention based use of magnification with a brightfield microscope). A microscope has multiple magnification settings that enable the user to view a specimen at different scales. Starting at the lowest magnification setting, the whole specimen can be observed. As the magnification is increased, the specimen is proportionally magnified, thereby providing finer detail while at the same time, a smaller part of the specimen is displayed. During a visual examination, the clinician finds areas of interest at lower magnification levels and then examines them further at higher and higher magnification levels, accruing in the process information from all magnification levels. Similarly, a MagNet starts at the lowest magnification level and recursively identifies, magnifies and analyses areas of interest with more fine-grain detail (see Figure 1). More importantly, as we show in our experiments, MagNets can be optimized without extra supervision (e.g. boundary boxes) for the task at hand.

MagNets provide a new way of solving both the “where” and “what” problems of gigapixel image analysis in an end-to-end fashion [10]. Given the innate transparency, no pre-processing requirements, and ability to perform both localization and classification tasks with no additional information (only slide-level information used [10]), it would be no exaggeration to say that MagNets have the potential to revolutionize fields, such as Digital Pathology.

The rest of the paper is organised as follows. In Section 2 we provide further context for gigapixel image analysis, and discuss related work. In Section 3, we introduce the key novelty of the present work, that is, explain the technical underpinnings of MagNets. In Section 4, we provide more details on the data, as well as the optimization framework. Finally, in Section 5, we discuss our results, and conclude our work with Section 6.

2. Related Work

Pathology is embracing the era of digitisation and, with the widespread adoption of whole slide scanners, has become a research area which stands to benefit greatly from advances in gigapixel image analysis on the one hand, and which presents novel challenges to computer vision and deep learning techniques, on the other.

3. Magnifying Networks

Large images typically require further preprocessing for any meaningful analysis. While a number of different approaches have been described in the literature, CNN based ones have emerged as the most effective and popular choice [12, 1] as a way of automatically learning features rather than handcrafting them. A CNN typically excels with image sizes of less than one million pixels [32, 15, 34, 39, 17]. Consequently, the most popular preprocessing approach to gigapixel image analysis involves the breaking up of the original large image into its constituent sub-images, that is patches, but also sometimes referred to as regions of interest (ROIs).

A challenge that comes with patch-based supervised training is the need for patch-level annotations. Although patch-level labelling can sometimes be provided [27, 37, 25, 22], it is generally either extremely laborious and expensive to obtain or simply infeasible. In order to make use of unlabelled patches, most of the existing approaches employ techniques from multiple instance learning (MIL) [16, 5, 3], weakly supervised learning [41, 2] and unsupervised learning [36].

In MIL, unlabelled instances belong to labelled bags of instances. The bag label can be determined based on a single instance [5], or based collectively on all the instances [16, 3]. In weakly supervised learning, mostly inexact supervision is observed in which the image-level (slide-level) label is used at some point as the patch-level label [41, 2]. Finally, there have also been some approaches that employ unsupervised learning techniques either as an early step in a pipeline [41] or as a way of compressing the gigapixel images into smaller representations [36].

One of the primary limitations of the previously described methods emerges as a consequence of their analysing a large input image by means of independent analysis of smaller patches that is divided into. In particular, such approaches are inherently unable to capture information distributed over scales greater than the patch size. For example in the case of whole slide images, although cell characteristics can be extracted based on isolated patches, higher-level structural information, such as the shape or extend of a tumour, can only be captured when analysing larger regions. Explicitly modeling the spatial correlations between the patches has been proposed as a potential solution [25, 22, 40]. A different approach involves the use of multi-resolution patches [11, 16, 27, 5] which seems to provide better empirical results.

Another major limitation of patch-based analysis comes from the initial patch extraction procedure. There are generally two ways that the WSIs are turned into patches: (a) by tiling the whole image or (b) by random sampling. On the one hand, the brute force nature of (a) is computational prohibiting which is why most methodologies resort to in-

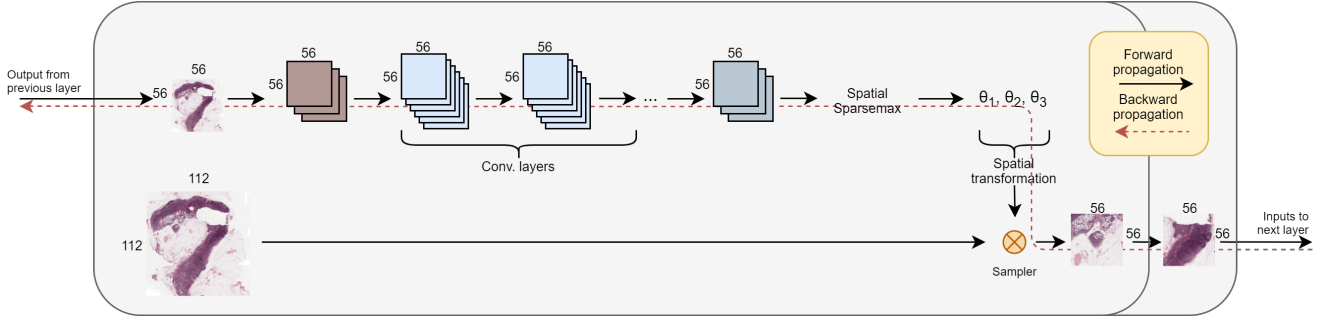


Figure 2. An illustration of a single magnifying layer that outputs two patches. The convolutional layers are independent between the two patches. Note that if this was the last magnifying layer, the image size of the patches would have been 224×224 .

tensive preprocessing steps. On the other hand, relevant information can be missed out with (b), especially since we are dealing with gigapixel images. A more sophisticated approach to selecting the right patches involve the use of attention models [2, 29, 28].

The framework we introduce in this paper addresses all of the aforementioned limitations. It allows for a multi-resolution, multi-field of view neural network to be optimized in an end-to-end fashion with gigapixel images, and without the need for any type of preprocessing. For the dynamic patch localization, we employ the Spatial Transformer Network (STN) [18] in a new way as described in the following section. The most prominent use cases of STNs are spatial invariance [31] and supervised semantic segmentation [20, 7, 14]. Existing research on MIL of STNs is scarce and, relative to our approach, simple [33, 13].

A MagNet consists of N magnifying layers followed by a classification layer. Consider a single gigapixel image I_0 that will pass through a MagNet.

3.1. Magnifying Layer

Resize and pad. As we subsequently employ convolutional layers expecting 56×56 pixel images, input I , either as a single input image (e.g. I_0) or a set of images, is resized to a $56 \times h_i$ or $w_i \times 56$ resolution with the smaller side, h_i or w_i , then padded (new pixels are black) so that $h_i = 56$ or $w_i = 56$ accordingly. For the purpose of up-sampling (see ‘‘Sampling’’ paragraph), a larger version I' (112×112 resolution) is also generated.

Convolutional layers. The salient parts in each image (e.g. areas with tissue at the lowest magnification level) vary significantly in size. This is illustrated in Figure 3 wherein each row depicts a different WSI. Therefore, the right kernel size for the convolutional operations varies depending on I . As such, we stack convolutional operations with different kernel sizes similarly to InceptionNet-v3 [35]. Further information is provided in the Appendix. Our MagNets employ three stacked convolutional layers for each patch

independently, e.g. a 2-layer MagNet with two patches at each magnifying layer has six of these layers (two at the first layer, and four at the second).

Spatial Transformer. A STN consists of three parts; a localization network, a grid generator, and a sampler [18].

The *localization network* is typically a FCNN or a recurrent neural network [33], and its role is to output the parameters of a spatial transformation. With scalability in mind, this approach was too prohibitive (GPU VRAM-wise) for MagNet as for each ST there would have been a large amount of extra parameters that needed to be optimized.

Instead, MagNet utilizes a spatial sparsemax at the last convolutional layer whose output can be used to infer the affine transformation parameters (s, t_x, t_y) directly (more information in Appendix). Note how the output of sparsemax has a 56×56 resolution and can therefore be thought as a mask highlighting the regions of interest of the input image.

Given the transformation parameters s for isotropic scaling and t_x, t_y for translation on each axis, we further constrain the parameters accordingly:

$$s = \max(s, 0.05) \quad (1)$$

$$t_x = \tanh(t_x) \quad (2)$$

$$t_y = \tanh(t_y) \quad (3)$$

for spatial (affine) transformation θ ,

$$\theta = \begin{bmatrix} s & 0 & t_x \\ 0 & s & t_y \end{bmatrix} \quad (4)$$

The *grid generator* then creates the desired grid by applying θ on a meshgrid with dimensions 56×56 . Based on a differentiable *sampler*, e.g. bilinear sampling, an image can be transformed by θ by interpolating it onto the grid.

Sampler Early on while experimenting with bilinear interpolation, it became obvious that it was a poor choice of

a sampler for our work. For more information we direct the reader to the excellent work of Jiang et al. [19] that later came out corroborating to our empirical analysis and providing an alternative sampler, called Linearized Multi-Sampling, whose gradients are not affected by the amount of scaling (i.e. how much the network has zoomed-in) that is needed (part of our empirical analysis is included in the Appendix). We use the original implementation of this sampler as provided to the authors by Jiang et al. [19].

Sampling (The “heart” of the MagNet) This is the part that makes each layer “magnifying”. Given θ and I , we can transform I based on θ (simple matrix operation) to retrieve an image containing only the detected region of interest. MagNet applies the transformation θ on I' instead, thereby allowing the output to contain information (finer-grain) that was not present in I . An example of a magnifying layer that outputs two patches is shown in Figure 2. The introduction of new information by transforming images that came from a higher magnification level is what enabled the idea of stacking multiple magnification layers together.

3.2. Classification Layer

The images of the last magnifying layer are sampled using a grid with 224×224 pixel resolution. These images are forwarded through a CNN (InceptionNet-v3) that outputs a feature map into a Gated Recurrent Unit (GRU) network. The output of the GRU can be passed through a FCNN (two layers with 512 and 256 hidden neurons respectively) to output the \hat{y} estimate of whether the given WSI contains cancer or not.

3.3. Auxiliary classifiers

A form of self-supervision is introduced by using two auxiliary classifiers. These are ImageNet-pretrained ResNets-18 networks [15] that output a slide-level prediction using the extracted images from magnifying layer 1 and layer 3 respectively. The premise is that information presented at layer 3 images should provide an equally good, or better, prediction than that from layer 1.

3.4. Configurations

The network consists of L magnifying layers each of which is concerned with a different magnification scale, shifted dynamically based on the degree of zooming (i.e. s) thus far. At each layer l , P_l number of patches are extracted (ROIs).

A consequence of the recurrent nature of MagNets is that an exponential number of patches are extracted and analysed from a single gigapixel image, if more than 1 patch is extracted per layer. In particular, given a constant P_l across the layers:

$$\text{Total patches} = \begin{cases} L, & \text{if } P = 1. \\ P^L, & \text{otherwise.} \end{cases}$$

We find that a combination of [2, 3] for P_l provides a balance between a sufficient rate of expansion (breadth), while allowing for up to 4-layer MagNets (depth) to be trained on a GPU with 24 GB of VRAM.

4. Evaluation

4.1. Camelyon data sets

The Camelyon data sets contain WSIs from surgically resected lymph nodes of breast cancer patients. These WSIs were independently curated across multiple hospitals [12, 26]. Camelyon16 includes images from 238 normal and 160 cancerous tissue sections whereas the publicly available portion of Camelyon17 has a total of 500 WSIs (318 normal, 182 cancerous). In addition, in the case of metastasis, metadata is available as to the extent of the metastasis (macrometastasis, micrometastasis, or isolated tumour cells (ITC)). Since only a small portion of the data set contains the much more difficult ITC cases, we exclude such cases from the training data set.

We follow the protocol described in the Camelyon competition website, and in addition set aside 25% of Camelyon17 as a testing set. We shuffle the remaining WSIs from Camelyon17 with the Camelyon16 WSIs, and train on the 80% and validate the better models from the remaining 20%. The best MagNets (based on the validation set) are retrained on both the training and validation data, and evaluated on the testing set.

The pixel-level annotations that are available for some of the WSIs of Camelyon are not used in our work. Instead, we only use the binary slide-level label that indicates the presence, or lack thereof, of cancerous cells somewhere in the gigapixel image.

4.2. Data Augmentation

For any given image, we apply a filter that removes the “grey” pixels of the image. This includes any white background, as well as gradients and other artifacts that have red, green, and blue channel values close together (threshold set to 15). The effects of the filter are illustrated in Figure 3.

We employ neither colour normalization nor random colour perturbation [27]. Synthetic data augmentation we perform is based on horizontal and vertical mirroring, and rotation by 90, 180, and 270 degrees.

4.3. Training

The networks were trained using the Adam optimizer for 200 epochs. A batch size of 16 and 8 was employed for

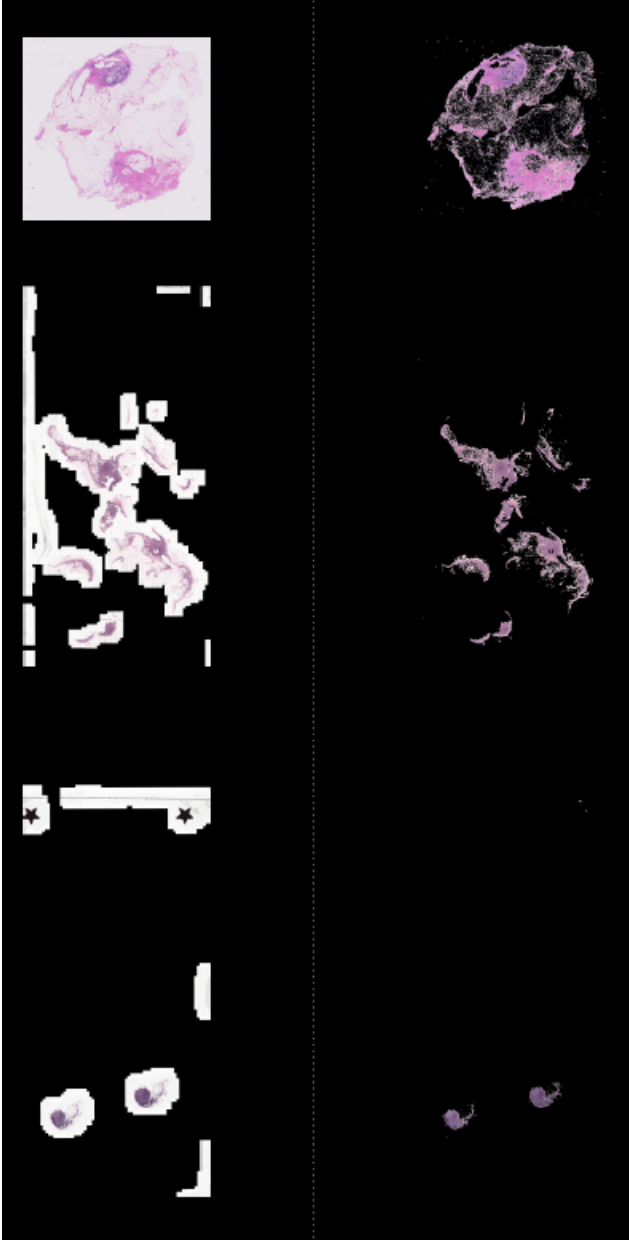


Figure 3. Three WSIs from different hospitals showcasing the differences in the scanning process. The left side shows the unfiltered version of the WSI, whereas the right side shows the WSIs after the “grey” filter has been applied.

MagNet networks with 3 and 4 layers respectively. The initial learning rate was set to 3×10^{-5} and was decayed using a cosine annealing scheduler. Both ResNet and InceptionNet networks are initialized using pretrained networks on ImageNet. However, the ST convolutional layers are randomly initialized.

“Frozen” patch Some WSIs have already been preprocessed so that they only contain regions with tissue, whereas others depict all of the tissue slide (see Figure 3). This diversity comes as a consequence of the differences in the clinical pipelines leading to the creation of WSIs, e.g. due to different scanning profiles. In order to mitigate for the above, we freeze the 1st patch of the 2nd layer so that it always attends to the whole input image. This allows for the image to catch-up in quality in the cases where a large amount of zooming was required at the first magnifying layer, i.e. when the WSI shows the whole tissue slide. Examples are included in the Appendix.

Loss Functions In order to impose the aforementioned self-supervision with the auxiliary classifiers, we employ the paradoxical loss function as described by Maksoud et al. [28]. In addition, cross-entropy is used between the slide-level labels and both the last output of the GRU as well as the ResNet-18 outputs.

5. Results & Discussion

To evaluate the proposed method, using the optimization framework described in the previous section we trained 3-layer and 4-layer MagNets on the task of cancer detection from WSIs. A summary of the results is presented in Table 1 which shows the area under the receiver operating characteristic curve (AUROC) – the standard evaluation metric used in the related literature [37, 36, 12, 26] – obtained using different configurations of the proposed method and the state of the art in the literature. Considering that to the best of our knowledge there is no existing work which utilizes only slide-level information on the Camelyon17 data set, the comparison in the table is made with the best reported competitor performances on Camelyon16 [36] (which would be fair to say overall provides a lesser challenge, thus, if anything, making the comparison disadvantageous to our method).

Interrogating our findings further, we note that although the 3-layer MagNet achieves better separation between macro-metastasis and normal cases, the 4-layer MagNet does better on micro-metastasis, as well as on the ITC cases. The latter is unsurprising given that a 4-layer MagNet makes use of finer-grain detail (cells are visible in Figure 5). Perhaps more importantly, the 4-layer MagNet performs well on ITC cases with a 63% AUROC despite the lack of ITC examples in our training set.

MagNets exhibit robust and effective exploration capabilities, namely attending to image content in an attention driven manner, exploring slides at varying magnification levels best suited to the task at hand and learning how to fuse relevant information both within the same WSI region and across different regions at different magnification levels. In addition, the classifier (in the form of Inception-



Figure 4. Examples from the testing set against the 3-layer MagNet. WSIs in the top square (blue) do not contain any malignancies, whereas the WSIs on the bottom (red) contain macro-, micro-metastasis, and ITC in order from top to bottom. The red circles show the cancer based on the annotations provided by the pathologists. Note that only 10 out of the last layer’s 18 patches are shown for space efficiency.

Net) demonstrates an excellent ability to distinguish normal from cancerous tissue across all magnifications. Examples corroborating this are shown in Figure 4. It is particularly

remarkable to observe cases such as those shown in rows 3–4 of the bottom group of examples in Figure 4, wherein the classifier can be seen to change its decision from “normal”

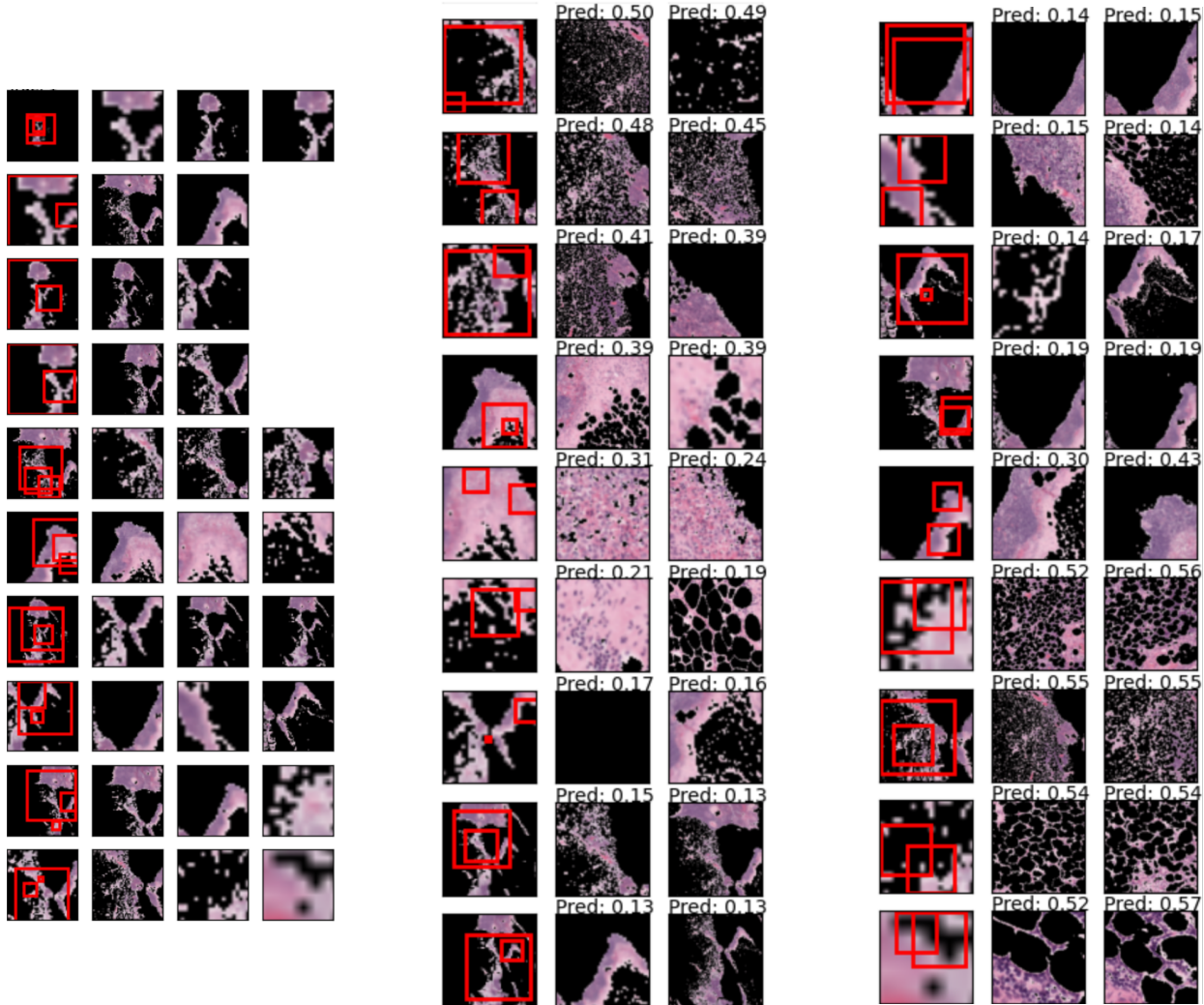


Figure 5. A visualization of a forward pass of a WSI with minor metastasis (from the testing set) through a 4-layer MagNet.

Table 1. The results of MagNets on the testing set containing 25% of the publicly available Camelyon17 data set.

	Macro-	Micro-	ITC	Macro + Micro	All
Mean RGB Baseline [36]	59%	57%	-	58%	-
Baseline w/ patch-level supervision [36]	91%	63%	-	77%	-
NIC [36]	72%	68%	-	70%	-
3-layer MagNet	95%	71%	57%	84%	71%
4-layer MagNet	91%	76%	63%	84%	75%

to “cancerous” when sufficient evidence for cancer is accumulated at any magnification level. These examples were verified by using annotations provided by pathologists.

Figure 5 shows the forward pass of a single example through a 4-layer MagNet. The Figure is made up of three images. Image A contains 10×4 sub-images wherein the first column contains the input I to a magnifying layer along red squares indicating the patches to be magnified next, as selected by the MagNet. The rest of the images visualize

the last magnifying layer along with its magnified patches of 224×224 pixel resolution that are forwarded to the classification layer. Since a GRU is employed in the classification layer, we are able to output a prediction with each new patch, allowing for trivial post-processing analysis. For instance, in the example shown, we observe that the model did not find anything that could be considered as a malignancy for the better part of the last layer’s patches. The patches responsible for the change in malignancy probability (from

0.19 to 0.30 and then 0.43) contain a region that was not seen in previous patches and which contains unusual looking tissue. As the final patches are forwarded through the GRU, we observe that the model successfully classifies the WSI as cancerous.

6. Conclusions

In this work, we introduced the MagNet – a neural network consisting of fully-connected, convolutional, and recurrent layers that employ spatial transformers (ST) in a novel and ingenious manner so as to facilitate attention and data driven recurrent exploration and, ultimately, end-to-end learning over gigapixel images. Our experimental results and analysis demonstrate the manifold novel capabilities of both the MagNets and the proposed framework in gigapixel image analysis.

The built-in hard attention mechanism of MagNets makes them perfectly suited for clinical use. In particular, any machine learning system that is deployed in clinical practice must generate accurate explanations for its decisions that are easily interpretable by a medical expert. The explanations generated by MagNets are visually intuitive for a domain-specific expert to interpret and can be generated on the go without any additional overhead. Moreover, MagNets can be optimized without extra supervision (e.g. bounding boxes) for the task at hand. This is of high significance since for most clinical tasks, collecting ground truth data required for a higher degree of supervision is either extremely laborious and expensive, or simply not possible, e.g. in the case of patient prognosis.

References

- [1] G. Aresta, T. Araújo, S. Kwok, S. S. Chennamsetty, M. Safwan, V. Alex, B. Marami, M. Prastawa, M. Chan, M. Donovan, G. Fernandez, J. Zeineh, M. Kohl, C. Walz, F. Ludwig, S. Braunewell, M. Baust, Q. Dang Vu, M. Nguyen Nhat To, and P. Aguiar. Bach: Grand challenge on breast cancer histology images. *arXiv:1808.04277*, 2018. [1](#), [2](#)
- [2] A. BenTaieb and G. Hamarneh. Predicting cancer with a recurrent visual attention model for histopathology images. In A. F. Frangi, J. A. Schnabel, C. Davatzikos, C. Alberola-López, and G. Fichtinger, editors, *Medical Image Computing and Computer Assisted Intervention*, pages 129–137. Springer International Publishing, 2018. [2](#), [3](#)
- [3] D. Bychkov, N. Linder, R. Turkki, S. Nordling, E. P. Kovanen, C. Verrill, M. Walliander, M. Lundin, C. Haglund, and J. Lundin. Deep learning based tissue analysis predicts outcome in colorectal cancer. *Scientific Reports*, 8(1), feb 2018. [2](#)
- [4] Peter D. Caie, Neofytos Dimitriou, and Ognjen Arandjelović. Chapter 8 - precision medicine in digital pathology via image analysis and machine learning. In Stanley Cohen, editor, *Artificial Intelligence and Deep Learning in Pathology*, pages 149–173. Elsevier, 2021. [1](#)
- [5] G. Campanella, W. K. V. Silva, and J. T. Fuchs. Terabyte-scale deep multiple instance learning for classification and localization in pathology. *arXiv:1805.06983*, 2018. [2](#)
- [6] Y. Chen, J. Li, H. Xiao, X. Jin, S. Yan, and J. Feng. Dual path networks. *CoRR*, abs/1707.01629, 2017. [1](#)
- [7] J. Dai, K. He, and J. Sun. Instance-aware semantic segmentation via multi-task network cascades. *CoRR*, abs/1512.04412, 2015. [3](#)
- [8] I. Demir, K. Koperski, D. Lindenbaum, G. Pang, J. Huang, S. Basu, F. Hughes, D. Tuia, and R. Raskar. Deepglobe 2018: A challenge to parse the earth through satellite images. *arXiv:1805.06561*, 2017. [1](#)
- [9] Jia Deng, Wei Dong, Richard Socher, Li-Jia Li, Kai Li, and Li Fei-Fei. Imagenet: A large-scale hierarchical image database. In *2009 IEEE Conference on Computer Vision and Pattern Recognition*, pages 248–255, 2009. [1](#)
- [10] Neofytos Dimitriou, Ognjen Arandjelović, and Peter D. Caie. Deep learning for whole slide image analysis: An overview. *Frontiers in Medicine*, 6:264, 2019. [1](#), [2](#)
- [11] S. Doyle, M. Feldman, J. Tomaszewski, and A. Madabhushi. A boosted bayesian multiresolution classifier for prostate cancer detection from digitized needle biopsies. *IEEE Transactions on Biomedical Engineering*, 59(5):1205–1218, may 2012. [2](#)
- [12] B. B. Ehteshami, M. Veta, P. Johannes van Diest, and et al. Diagnostic assessment of deep learning algorithms for detection of lymph node metastases in women with breast cancer. *JAMA*, 318(22):2199–2210, 2017. [1](#), [2](#), [4](#), [5](#)
- [13] S. Guo, L. Liu, W. Wang, S. Lao, and L. Wang. An attention model based on spatial transformers for scene recognition. In *2016 23rd International Conference on Pattern Recognition (ICPR)*, pages 3757–3762, 2016. [3](#)
- [14] K. He, G. Gkioxari, P. Dollár, and B. R. Girshick. Mask R-CNN. *CoRR*, abs/1703.06870, 2017. [3](#)
- [15] Kaiming He, Xiangyu Zhang, Shaoqing Ren, and Jian Sun. Deep residual learning for image recognition. In *2016 IEEE Conference on Computer Vision and Pattern Recognition (CVPR)*, pages 770–778, 2016. [1](#), [2](#), [4](#)
- [16] L. Hou, D. Samaras, M. T. Kurc, Y. Gao, E. J. Davis, and H. J. Saltz. Patch-based convolutional neural network for whole slide tissue image classification. In *2016 IEEE Conference on Computer Vision and Pattern Recognition (CVPR)*. IEEE, jun 2016. [2](#)
- [17] G. Huang, Z. Liu, and Q. K. Weinberger. Densely connected convolutional networks. *CoRR*, abs/1608.06993, 2016. [1](#), [2](#)
- [18] M. Jaderberg, K. Simonyan, A. Zisserman, and K. Kavukcuoglu. Spatial transformer networks. *CoRR*, abs/1506.02025, 2015. [1](#), [3](#)
- [19] Wei Jiang, Weiwei Sun, Andrea Tagliasacchi, Eduard Trulls, and Kwang Moo Yi. Linearized multi-sampling for differentiable image transformation. In *Proceedings of the IEEE/CVF International Conference on Computer Vision (ICCV)*, 2019. [4](#)
- [20] J. Johnson, A. Karpathy, and F. F. Li. Denscap: Fully convolutional localization networks for dense captioning. *CoRR*, abs/1511.07571, 2015. [3](#)

- [21] W. Kay, J. Carreira, K. Simonyan, B. Zhang, C. Hillier, S. Vijayanarasimhan, F. Viola, T. Green, T. Back, P. Natsev, M. Suleyman, and A. Zisserman. The kinetics human action video dataset. *CoRR*, abs/1705.06950, 2017. 1
- [22] Bin Kong, Xin Wang, Zhongyu Li, Qi Song, and Shaoting Zhang. Cancer metastasis detection via spatially structured deep network. In Marc Niethammer, Martin Styner, Stephen Aylward, Hongtu Zhu, Ipek Oguz, Pew-Thian Yap, and Dinggang Shen, editors, *Information Processing in Medical Imaging*, pages 236–248. Springer International Publishing, 2017. 2
- [23] A. Kuznetsova, H. Rom, N. Alldrin, J. Uijlings, I. Krasin, J. Pont-Tuset, S. Kamali, S. Popov, M. Mallocci, T. Duerig, and V. Ferrari. The open images dataset v4: Unified image classification, object detection, and visual relationship detection at scale. *arXiv:1811.00982*, 2018. 1
- [24] G. Larsson, M. Maire, and G. Shakhnarovich. Fractalnet: Ultra-deep neural networks without residuals. *CoRR*, abs/1605.07648, 2016. 1
- [25] Y. Li and W. Ping. Cancer metastasis detection with neural conditional random field. *arXiv:1806.07064*, 2018. 2
- [26] G. Litjens, P. Bandi, B. Ehteshami Bejnordi, O. Geessink, M. Balkenhol, P. Bult, A. Halilovic, M. Hermsen, R. van de Loo, R. Vogels, F. Q. Manson, N. Stathonikos, A. Baidoshvili, P. van Diest, C. Wauters, M. van Dijk, and J. van der Laak. 1399 h&e-stained sentinel lymph node sections of breast cancer patients: the CAMELYON dataset. *GigaScience*, 7(6), May 2018. 1, 4, 5
- [27] Y. Liu, K. Gadepalli, M. Norouzi, E. G. Dahl, T. Kohlberger, A. Boyko, S. Venugopalan, A. Timofeev, Q. P. Nelson, S. G. Corrado, D. J. Hipp, L. Peng, and C. M. Stumpe. Detecting cancer metastases on gigapixel pathology images. *CoRR*, abs/1703.02442, 2017. 2, 4
- [28] Sam Maksoud, Kun Zhao, Peter Hobson, Anthony Jennings, and Brian C. Lovell. Sos: Selective objective switch for rapid immunofluorescence whole slide image classification. In *Proceedings of the IEEE/CVF Conference on Computer Vision and Pattern Recognition (CVPR)*, June 2020. 3, 5
- [29] T. Qaiser and M. N. Rajpoot. Learning where to see: A novel attention model for automated immunohistochemical scoring. *arXiv*, 2019. 3
- [30] S. Sabour, N. Frosst, and E. G. Hinton. Dynamic routing between capsules. *CoRR*, abs/1710.09829, 2017. 1
- [31] C. Shu, X. Chen, Q. Xie, and H. Han. Hierarchical spatial transformer network. *CoRR*, abs/1801.09467, 2018. 3
- [32] K. Simonyan and A. Zisserman. Very deep convolutional networks for large-scale image recognition. *CoRR*, abs/1409.1556, 2014. 1, 2
- [33] K. S. Sønderby, K. C. Sønderby, L. Maaløe, and O. Winther. Recurrent spatial transformer networks. *CoRR*, abs/1509.05329, 2015. 3
- [34] C. Szegedy, W. Liu, Y. Jia, P. Sermanet, E. R. Reed, D. Anguelov, D. Erhan, V. Vanhoucke, and A. Rabinovich. Going deeper with convolutions. *CoRR*, abs/1409.4842, 2014. 1, 2
- [35] Christian Szegedy, Vincent Vanhoucke, Sergey Ioffe, Jonathon Shlens, and Zbigniew Wojna. Rethinking the inception architecture for computer vision, 2015. 3
- [36] David Tellez, Geert Litjens, Jeroen van der Laak, and Francesco Ciompi. Neural image compression for gigapixel histopathology image analysis. *IEEE Transactions on Pattern Analysis and Machine Intelligence*, 43(2):567–578, 2021. 2, 5, 7
- [37] D. Wang, A. Khosla, R. Gargeya, H. Irshad, and H. A. Beck. Deep learning for identifying metastatic breast cancer. *arXiv:1606.05718*, 2016. 2, 5
- [38] X. Yue, N. Dimitriou, and O. Arandjelović. Colorectal cancer outcome prediction from H&E whole slide images using machine learning and automatically inferred phenotype profiles. *BICOB*, pages 139–149, 2019. 1
- [39] S. Zagoruyko and N. Komodakis. Wide residual networks. *CoRR*, abs/1605.07146, 2016. 1, 2
- [40] G. F. Zanjani, S. Zinger, and H. N. P. de With. Cancer detection in histopathology whole-slide images using conditional random fields on deep embedded spaces. In *Medical Imaging 2018: Digital Pathology*. SPIE, mar 2018. 2
- [41] X. Zhu, J. Yao, F. Zhu, and J. Huang. Wsisa: Making survival prediction from whole slide histopathological images. In *2017 IEEE Conference on Computer Vision and Pattern Recognition (CVPR)*, pages 6855–6863, July 2017. 2